Available online at www.sciencedirect.com
ScienceDirect
Electrochimica Acta 52 (2007) 6282–6294
ELECTROCHIMICA Acta
www.elsevier.com/locate/electacta

Chalcogenide electrocatalysts for oxygen-depolarized aqueous hydrochloric acid electrolysis

Joseph M. Ziegelbauer [a], Andrea F. Gullá [b], Cormac O'Laoire [a], Christian Urgeghe [a,1], Robert J. Allen [b], Sanjeev Mukerjee [a,*]

[a] *Northeastern University, Department of Chemistry and Chemical Biology, Boston, MA 02115, USA*
[b] *E-TEK Division of PEMEAS, 39 Veronica Avenue, Somerset, NJ 08873, USA*

Received 28 February 2007; received in revised form 10 April 2007; accepted 11 April 2007
Available online 24 April 2007

Abstract

Several Rh- and Ru-based carbon-supported chalcogenide electrocatalysts were evaluated as oxygen-depolarized cathodes for HCl electrolysis applications. The roles of both crystallinity and morphology of the electrocatalysts were explored by investigating several synthetic processes for materials, specifically patented *E-TEK* methods and the non-aqueous method. The activity of the electrocatalysts for ORR was evaluated via RDE studies in 0.5 M HCl, and compared to state of the art Pt/C and Rh/C systems. Rh_xS_y/C, $Co_xRu_yS_z$/C, and Ru_xS_y/C materials synthesized from the *E-TEK* methods exhibited appreciable stability and activity for ORR under these conditions. The amorphous non-aqueous moieties, while exhibiting little depolarization due to the presence of high concentrations of Cl^- in the RDE studies, were unsuitable for operation in a true ODC HCl electrolyzer cell because of irreversible dissolution resulting from the high concentration (∼5 M) of HCl. In contrast, the Ru-based materials from the *E-TEK* methods were unaffected by the depolarizing conditions of an uncontrolled shutdown. These Ru-based electrocatalysts, being on the order of seven times less expensive than the state of the art Rh_xS_y material, may prove to be of economic benefit to the HCl electrolysis industry.

Keywords: Oxygen-depolarized electrode; HCl electrolysis; Chalcogenides; Rhodium sulfide; Ruthenium sulfide

1. Introduction

Aqueous hydrochloric acid and chlorine are abundant chemicals in industry, especially in the context of the electrolysis of aqueous hydrochloric acid (HCl) for the recovery of high-value chlorine gas. This importance of this process is especially important in light of the recent workshop on "Approaches to Combat Terrorism" held in Washington, DC, 19–21 November 2002, where large storage tanks of chlorine gas present at industrial plants present attractive targets [1]. A general outline of a fully integrated electrolyzer process involves recycling the chlorine gas evolved in the anodic compartment of the cell for utilization as feedstock to the chemical plant. In the most basic form, this process can be accomplished electrolytically as

$$\text{Cathode}: \quad 2H^+ + 2e^- \leftrightarrow H_{2(g)} \quad E = 0.00\,\text{V versus RHE} \tag{1}$$

$$\text{Anode}: \quad 2Cl^- \leftrightarrow Cl_{2(g)} + 2e^- \quad E = -1.36\,\text{V} \tag{2}$$

$$\text{Overall}: \quad 2HCl \leftrightarrow 2H_{2(g)} + 2Cl_{2(g)} \quad E = -1.36\,\text{V} \tag{3}$$

Under ideal conditions, this process yields a metric ton of $Cl_{2(g)}$ with a power consumption of ∼1500 kW h. While feasible, the energy consumption coupled with safety concerns arising from the generation of $H_{2(g)}$ poses serious drawbacks. For example, an uncontrolled shutdown of the cell results in the $H_{2(g)}$-containing cathode compartment being flooded with concentrated Cl^- and $Cl_{2(g)}$ with potentially explosive results. One solution to these concerns is the oxygen-depolarized cathode (ODC) process of electrolytic $Cl_{2(g)}$ generation [2]. In this process, the cathodic reduction of protons to $H_{2(g)}$ is replaced

* Corresponding author. Tel.: +1 617 373 2382; fax: +1 617 373 8949.
E-mail address: s.mukerjee@neu.edu (S. Mukerjee).
[1] Current address: Industrie De Nora S.p.A., Via Bistolfi 35, 20134 Milan, Italy.

0013-4686/$ – see front matter © 2007 Published by Elsevier Ltd.
doi:10.1016/j.electacta.2007.04.048

with the oxygen reduction reaction (ORR) as thus

$$\text{Cathode}: \quad O_{2(g)} + 4H^+ + 4e^- \leftrightarrow 2H_2O_{(l)} \quad E = 1.23\,V \tag{4}$$

$$\text{Overall}: \quad 2HCl + 1/2O_2 \leftrightarrow Cl_{2(g)} + H_2O_{(l)} \quad E = -0.13\,V \tag{5}$$

with a theoretical energy savings of ~700 kW h per ton of $Cl_{2(g)}$.

Platinum is generally recognized as the most effective catalyst for ORR, especially in the low to medium temperature range acid environments of PEM fuel cells and electrolyzers [3]. However, in the particular case of aqueous HCl electrolysis, the use of a platinum-based catalyst as the cathode poses some serious drawbacks. For example, platinum is severely depolarized due to chloride anion adsorption, [4] and, to a lesser extent, by the surface reactions of omnipresent dissolved organic compounds [5]. Because of these factors, extreme precautions are necessary when performing periodic cell "shut-downs". In these situations, the sudden shift in the cathodic potential, combined with highly aggressive chemical environment ($Cl_{2(g)}$-saturated HCl), will result in both an irreversible dissolution of a significant amount of the platinum and a nearly complete deactivation of the remaining portion. While special procedures to overcome such catastrophic events are generally observed during planned shut-downs, nothing can be done in the case of an uncontrolled event (e.g., power shortage of the electrical network).

Efforts to avoid the instability of platinum in these electrolyzer systems lead to the development of a rhodium-based chalcogenide electrocatalyst (Rh_xS_y) pioneered by *E-TEK* Inc. (a division of PEMEAS Fuel Cell Technologies, Inc.) in early 2000 [6]. Despite a lower activity for oxygen reduction relative to state of the art Pt-based electrocatalysts in most systems, Rh_xS_y is not severely depolarized by contaminants such as chloride ions and assorted organics [5–7]. As a result of these exceptional performance gains, the Rh_xS_y electrocatalyst is being incorporated into a +1000 m^2 chlorine production plant [8]. Although these materials perform well in terms of activity and chemical resistance, price and availability are difficult issues to resolve in terms of large commercial applications. Recent spots prices[9] (per troy ounce of metal, ~31 g) for rhodium, platinum, and ruthenium were $6000, $1200, and $700 USD, respectively. Although depolarized aqueous hydrochloric acid electrolysis technologies have a high market demand, the price of the state-of-the-art Rh_xS_y catalyst may be too high for successful commercialization.

Transition metal-based chalcogenides represent an interesting class of alternative electrocatalysts for ORR applications. Chevrel-phase M_6Se_8 or M_6S_8 (M = transition metal compounds) are well established catalysts for hydrodesulfurization, hydronitrogenation, hydrodeoxygenation and hydrogenation reactions in industrial oil-refining applications [10–13]. Indeed, the initial models of chalcogenide clusters for ORR applications reported by Alonso-Vante and Tributsch were based on these Chevrel-phase clusters, where the metal atoms were octahedrally coordinated in a face-centered-cubic cell with the respective chalcogenide atoms located at the periphery [14,15]. Over the years, amorphous nanoparticles of Ru_xS_y and Ru_xSe_y synthesized via a low temperature non-aqueous route [16] have been touted as the state of the art electrocatalysts in this class [17,18]. In contrast to pyrite-type MS_2 varieties (typically RuS_2) utilized in industrial catalysis, these materials exhibit a fairly robust activity for ORR, even in high methanol-content environments [11,18]. As a result, a large variety of compounds have been proposed for ORR applications in acid electrolyte [17–20]. Despite their promising performance in PEMFC and DMFC applications, the activities of these materials in oxygen-depolarized chlorine-saturated electrolyzer applications have yet to appear in literature.

In this work, we will contrast and compare the activities of a variety of carbon-supported 30 wt.% Ru- and Rh-based sulfide ODC cathode for the production of chlorine gas via the electrolysis of HCl. Sulfur was the chalcogen of choice for three main reasons: (1) the solubility of Se and Te present major difficulties in the non-aqueous synthetic route, (2) gaseous sources of Se or Te (e.g., $H_2Se_{(g)}$) are not only highly expensive, but present significant safety issues, and (3) Se and Te are highly toxic and thus unattractive to industry from a variety of standpoints. Three synthetic methodologies were explored to produce "binary" Rh_xS_y and Ru_xS_y materials. In addition some of the more popular Mo, Co, Rh, and Re-doped Ru_xS_y catalysts championed for acid electrolyte fuel cell ORR applications were also prepared. Standard morphological characterization techniques were incorporated with electrochemical studies in 0.5 M HCl to screen the ORR activity and stability of the materials. The most promising candidates were then evaluated in a standardized, state of the art hydrochloric acid electrolyzer cell to evaluate performance in real world conditions. It is the objective of this report to evaluate alternative ruthenium-based chalcogenide electrocatalysts, in respect to their synthetic methodologies and resulting morphologies, for ODC catalysts in a chlorine-saturated hydrochloric acid environment in respect to both economic and industrial considerations.

2. Experimental

2.1. Material synthesis

2.1.1. Non-aqueous synthesis (NA) [16]

$Mo_xRu_yS_z$, $Rh_xRu_yS_z$, $Re_xRu_yS_z$, and Rh_xS_y electrocatalysts were synthesized via the so-called non-aqueous route [16]. The respective metal carbonyls (98–99.5%, Alfa Aesar) were combined with elemental sulfur (99.999%, Alfa Aesar) in a 3-neck flask in an argon-filled glovebox, and transferred to a fume hood. While flushing the flask with argon, de-aerated xylenes (HPLC grade, Aldrich) were transferred via a cannula in respect to the solubility of the metal carbonyls. The system was then refluxed under argon at ~145 °C for 20 h. Carbon black (Vulcan XC-72R, Cabot Corporation) was then added in a proportion to achieve a 30 wt.% (metal-basis) loading. After stirring at 120 °C for 3 h, the material was vacuum filtered, washed with copious amounts of acetone, and allowed to air dry in the fume hood overnight. Because of the solubility of the

respective metal carbonyl precursors, the total yields averaged only about 200 mg of 30 wt.% catalyst per synthesis. The target compositions were 1:1.5 M:Ru for the ternary compounds.

2.1.2. Gas–solid state reaction (SS)

Two samples, $Co_xRu_yS_z$ and Ru_xS_y, were synthesized via the gas–solid reaction, and are denoted in the text as the "SS" variety. Using $Co_xRu_yS_z$ as an example, stoichiometric quantities of ruthenium trichloride (Johnson Matthey) and cobalt nitrate were incorporated onto carbon (Vulcan XC-72R) by the incipient wetness procedure. This was followed by thermal treatment at high temperatures in an atmosphere of hydrogen sulfide (H_2S, 50%) and nitrogen (N_2, 50%).

2.1.2.1. Aqueous synthesis (AS) [6,7,21]. The Rh_xS_y (supplied by *E-TEK*) synthesized via this method is denoted in the text with an "AS" suffix. The synthesis begins with dispersing carbon black (Vulcan XC-72R) into a solution of rhodium trichloride. Sulfonation of the metal moiety was accomplished by bubbling a mixture of H_2S (60%) and N_2 (40%). After vacuum filtering with copious amount of de-ionized water and dried overnight under vacuum at 80 °C, the catalyst was heat treated in an inert atmosphere as outlined in the salient patent [7].

2.1.3. Sulfur ion-free synthesis (SF) [22]

A second portion of Rh_xS_y (supplied by *E-TEK*) was synthesized via the new "Sulfur Ion-free Synthesis", and is denoted in the text with an "SF" suffix. The synthetic procedure and work-up is identical to the AS process except that sulfonation is achieved by the judicious addition of thio-containing compounds until a stable pH is reached. The filtered and dried material is then heat treated in a manner identical to the AS method.

2.2. Morphological characterizations

2.2.1. X-ray diffraction (XRD) and scanning electron microscopy (SEM)

XRD spectra were obtained with a Rigaku D/MAX-2000 series diffractometer utilizing Cu $K\alpha_1$ radiation ($\lambda = 1.5406$ Å). Fast scans at 1° (2θ/min) were conducted to ensure the absence of extraneous phases, and were followed by slow scans to allow a detailed analysis of the lattice parameters of the crystal systems over 20–90° (2θ) when applicable. Select highly amorphous samples (Rh_xS_y/C, $Rh_xRu_yS_z$/C, and $Re_xRu_yS_z$/C, all NA) were examined with high intensity synchrotron radiation at the capillary X-ray diffraction beamline (X-7B) at the National Synchrotron Light Source (Brookhaven National Labs, Upton, NY). The synchrotron radiation was monochromated to $\lambda = 0.92137$ Å via a graphite monochromator, and the sample placed 175 mm from the X-ray source. The respective diffractograms are adjusted to Cu $K\alpha_1$ wavelength for comparative purposes. The quality of the electrocatalyst particle distributions and stoichiometries were evaluated with a model 5800 Hitachi Field Emission SEM/EDAX. Micrographs and EDAX were collected at 4, 5, and 20 keV over randomly chosen areas.

2.3. Electrochemical preparation and procedures

2.3.1. Rotating disk electrode (RDE)

RDE measurements were performed using a standard three electrode-electrochemical cell with an Ecochemie Autolab® PGSTAT30 (Brinkmann Instruments, Inc.) potentiostat/galvanostat. The electrolyte was prepared from HPLC grade HCl (Aldrich) and 18.2 MΩ water (Millipore, Inc.). As previously reported, [23,24] the working electrodes were prepared from a suspension of 6.83 mg of the respective catalyst (all 30 wt.% metal-basis), 10 ml of 1:1 vol.% 2-propanol (HPLC grade, Fisher):deionized water, and 40 μl of 5 wt.% Nafion® solution (Aldrich). After stirring at room temperature for 2 h, the ink was sonicated in an ultrasonic bath at room temperature for 10 min. The ink was applied to a 6 mm diameter glassy carbon disk (Pine Instrument Co.) via two 10 μl aliquots, and dried in ambient air after each application. The nominal loadings for all the examined electrocatalysts were 16 μg metal cm^{-2} (geometric). The resulting films exhibited good mechanical stability with negligible film diffusion effects [25]. An Ag/AgCl electrode ($E = -0.249$ V versus RHE in 0.5 M HCl), separated from the working electrode compartment by a fine glass frit to eliminate junction potentials, was utilized as the reference electrode. All reported potentials are in respect to a relative hydrogen electrode (RHE). The rotation rate of the RDE was controlled with a Pine Instrument Analytical Rotator (Model AFASR, Pine Instrument Co.). Before each electrode preparation, the glassy carbon electrode was polished to a mirror-finish using alumina (1.0 and 0.05 μm, Buehler). A platinum wire (99.9%, Alfa Aesar) served as the counter electrode.

Each catalyst was activated by cycling at 50 mV s^{-1} in de-aerated (ultrahigh purity Argon, MedTech Gases, Inc.) electrolyte until the material achieved a steady state. To avoid oxidative dissolution of the respective electrocatalysts, the following potential windows were utilized: (1) Pt: 1.25–0.01 V, (2) Rh-based: 1.2–0.01 V, and (3) Ru-based: 0.85–0.01 V. The room temperature RDE experiments were conducted using a scan rate of 20 mV s^{-1} under full O_2 saturation (MedTech).

2.3.2. HCl electrolyzer cell

While the overall design of the HCl electrolyzer cell roughly resembles that of a standard PEM or DMFC, there are a number of significant differences which will be briefly outlined here. The ODC cathodes were prepared by hand painting successive coatings of a catalyst/Teflon®/2-propanol slurry onto a carbon cloth (Zoltek Companies Inc, St. Louis, MO). After drying (80 °C vacuum oven between coatings) the 6.5 cm^2 electrodes possessed a metal loading of 5 mg cm^{-2}. Prior to contacting the electrode with the moistened Nafion® 362 membrane, the electrodes were coated with 0.5–0.8 mg cm^2 (dry Nafion®) of a 10 wt.% Nafion® perfluorocarbon ionomer solution. The Nafion® 362 membrane was developed for chlor-alkali applications, and is essentially a Nafion® membrane encapsulating a porous PTFE-coated fiberglass sheet for added mechanical stability with an overall thickness of ∼1 mm. The ODCs were then physically contacted to the Nafion® membrane (not hot pressed) by tightening down the Ti mesh current collector. This

is a standard industrial design where the replacement of the ODC after ∼10,000 h of operation while leaving the membrane and anode intact is an unchallengeable requirement.

The state of the art dimensionally stabilized anodes [26] utilized in the cell are commercially available from *E-TEK*. DSA electrodes have a long history of development, [27–29] and suppress the parasitic process of water electrolysis at the anode. In lieu of graphite, the entire cell (also supplied by *E-TEK*) was constructed of titanium-coated metals to better withstand the corrosive environs, and overviews of the design and principles of operation are readily available [30,31]. Akin to the cathodes, the anodes were also contacted to the Nafion® membrane by mechanical force only. As with the ODC, a Ti mesh was incorporated as the current collector. In addition, small DSA strips were incorporated into both the ODC and anode compartments to function as pseudo reference electrodes (∼−650 mV versus RHE).

Following assembly, the cathode compartment was fed pure O_2 at a backpressure of 2 atm while the anode received a feed of Cl_2-saturated HCl (184 g HCl l^{-1}). After slowly heating the cell to 55 °C, the conditions were maintained for 3 h prior to polarization. Polarization curves were obtained by holding the cell at the desired current density for 3 min before making a potential measurement. The effect of uncontrolled shutdowns on the cathode electrocatalysts was evaluated by simply switching off the cell during operation. After 12 h, the cell was restarted according to the conditions stated above, and returned to a constant current density.

3. Results and discussion

3.1. Morphological characterizations

3.1.1. Standard 30 wt.% Pt/C and Rh/C

Fig. 1 presents the X-ray diffractograms for the standard 30 wt.% Pt/C and Rh/C electrocatalysts supplied by *E-TEK*, Inc.

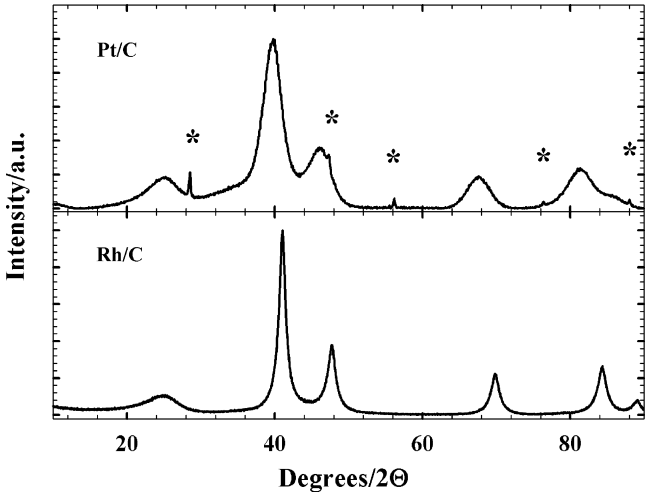

Fig. 1. Powder X-ray diffractograms of the 30 wt.% Pt/C (top) and 30 wt.% Rh/C (bottom) standard electrocatalysts from *E-TEK*. Asterisks indicate diffraction peaks from an incorporated silicon powder standard utilized for alignment. Cu Kα radiation, λ = 1.5406 Å.

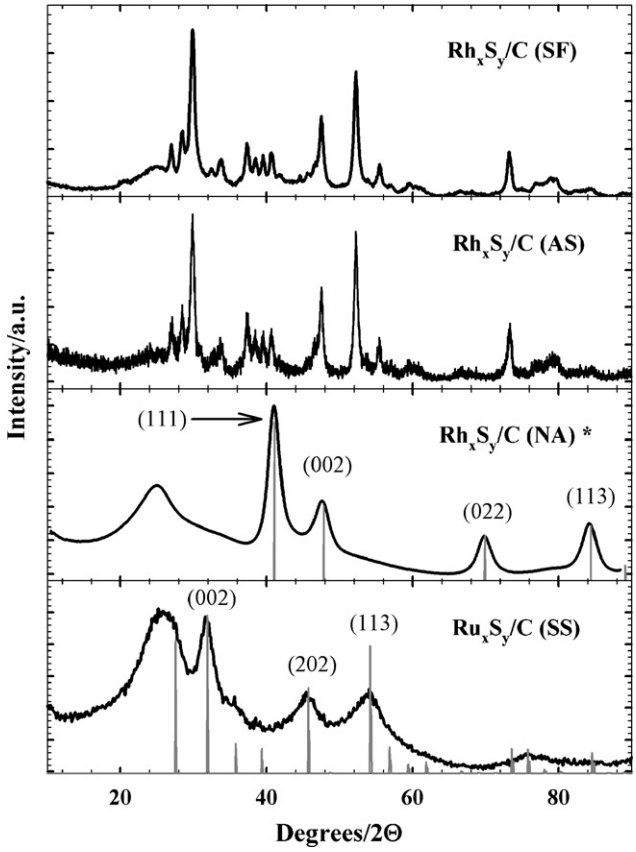

Fig. 2. Non-background-corrected powder X-ray diffractograms of 30 wt.% binary chalcogenide electrocatalysts (top to bottom): Rh_xS_y/C (SF), Rh_xS_y/C (AS), Rh_xS_y/C (NA), and Ru_xS_y/C (SS). Cu Kα radiation, λ = 1.5406 Å, except for Rh_xS_y/C (NA)*, which was performed at beamline X-7B (NSLS) with monochromated 0.92137 Å radiation (adjusted to Cu Kα λ for comparative purposes).

Both spectra are perfect representations of fcc (*Fm*3*m*) Pt and Rh. Application of the Debye-Scherrer technique to the primary (1 1 1) reflections yielded crystallite sizes of 3.2 and 8.4 Å for the Pt/C and Rh/C, respectively.

3.1.2. Binary chalcogenide electrocatalysts

X-ray diffractograms for the 30 wt.% Rh_xS_y/C (SF), Rh_xS_y/C (AS), Rh_xS_y/C (NA), and Ru_xS_y/C (SS) chalcogenide electrocatalysts are presented in Fig. 2. Considering that the Rh_xS_y (NA) diffractogram was obtained with high intensity synchrotron radiation (λ = 0.92137 Å), it is immediately apparent that the NA variety of Rh_xS_y/C exhibits a much lower degree of complexity than its SF and AS brethren. Both the SF and AS Rh_xS_y/C catalysts are known to be a balanced phase mixture [32] of at least three Rh–S phases: orthorhombic *Pbcn* Rh_2S_3, [33] monoclinic $C_{2/m}$ Rh_3S_4, [32,34] and primitive cubic *Pm*3*m* $Rh_{17}S_{15}$ [35,36]. Rh_2S_3 is an electronic insulator built of alternating RhS_6 octahedra. The average Rh–Rh bond distance of 3.208 Å (compared to 2.69 Å in fcc Rh metal) thus removes any possibility of direct Rh–Rh bonding. In contrast, the $Rh_{17}S_{15}$ phase possesses semiconductor properties at room temperature. In addition, $Rh_{17}S_{15}$ consists of Rh_8 octahedra with an average Rh–Rh distance of 2.59 Å. Previous *in situ* X-ray Absorption Spectroscopy and

Table 1
Particle size and morphology determinations

Catalyst	XRD particle size (Å)[a]	XRD indexing	SEM aggregate size (Å)	EDX stoichiometry M1:M2:S (±0.08)
Pt/C	3.2	*Fm*3*m* Pt	–	–
Rh/C	8.3	*Fm*3*m* Rh	–	–
Rh_xS_y/C (SF)	–	balanced phase[b]	10–26	1.1:1.0
Rh_xS_y/C (AS)	–	balanced phase[b]	12–30	1.1:1.0
Rh_xS_y/C (NA)	3.2	*Fm*3*m* Rh	3–4	1.1:1.0
Ru_xS_y/C (SS)	6.4	*Pa*3 (RuS_2)	6–12	1.0:2.2
$Co_xRu_yS_z$/C (SS)	8.8	*Pa*3 (RuS_2)	10–18	0.3:0.7:2.3
$Mo_xRu_yS_z$/C (NA)	2.2	*P*6(3)/*mmc* Ru	2–6	0.9:1.9:5.0
$Rh_xRu_yS_z$/C (NA)	2.2[c]	*P*6(3)/*mmc* Ru	2–5	1.0:1.5:5.0
$Re_xRu_yS_z$/C (NA)	2.4[c]	*P*6(3)/*mmc* Ru	2–5	0.9:1.7:5.0

[a] Debye-Scherrer Analysis, ±0.2 Å.
[b] Balanced phase of Rh_2S_3, Rh_3S_4, and $Rh_{17}S_{15}$, see Refs. [32,33,35].
[c] Exhibits reflections from dopants, see text.

electrochemical studies [37,38] have shown the Rh_3S_4 phase, with its metallic Rh_6 octahedra eaves, is the active site for O(H) adsorption. Both the SF and AS Rh_xS_y/C XRD spectra are dominated by the $Rh_{17}S_{15}$ phase with a characteristic set of four peaks at $2\theta = 37.38$–40.68° representing the (1 0 4), (1 1 4), (2 2 3), and (0 2 4) reflections, and the high intensity peaks at 47.64 and 52.16° indicating the (3 3 3) and (0 4 4) reflections. The Rh_2S_3 and Rh_3S_4 phases are completely amorphous at the 30 wt.% loading although a recent study has shown that the phase balance can be altered by adjusting the overall Rh_xS_y loading on the carbon support [39]. In contrast, this considerable level of complexity is eliminated by synthesizing the Rh_xS_y/C material via the low temperature NA route. The spectrum for Rh_xS_y/C (NA) in Fig. 2, performed with high intensity synchrotron radiation at the National Synchrotron Light Source's beamline X-7B (Brookhaven National Labs, Upton, NY), shows a powder XRD spectrum indicative of 3.2 nm fcc Rh crystallites (grey lines under the Rh_xS_y/C (NA) spectrum). This is not unexpected, for the NA synthetic route typically produces small (~2–4 nm) amorphous nanoparticles [17,40,41]. In addition, EDX analysis of the as-synthesized Rh_xS_y/C electrocatalysts show roughly the same 1.1:1 Rh:S atomic ratio (Table 1) suggesting that the Rh nanoparticles are coated with an excess of sulfur [42]. Finally, the spectrum for the 30 wt.% Ru_xS_y/C electrocatalyst synthesized via the solid state $H_2S_{(g)}$ disproportionation route is given at the bottom of Fig. 2. The spectrum indicates that the crystallinity in the Ru–S can be attributed to a pyrite-type (*Pa*3) Ru(IV)S_2 structure (grey lines), specifically the (0 0 2), (2 0 2), and (1 1 3) reflections at 31.9, 45.7, and 54.21° 2θ, respectively. Considering the SS synthetic route, which involves a ~4 h thermal treatment at +350 °C in the presence of $H_2S_{(g)}$, it is not unexpected that the Ru–S would preferentially order into the pyrite-type laurite analogue. Again, however, EDX investigations of the as-synthesized material (Table 1) show a non-stoichiometric Ru:S atomic ratio of 1:2.2 where 1:2 would be expected for laurite. This again indicates either the presence of non-crystalline Ru–S phases or a coating of excess sulfur resulting from the non-stoichiometric addition of $H_2S_{(g)}$ during the synthesis.

3.1.3. Ternary chalcogenide electrocatalysts

Powder X-ray diffractograms of the $M_xRu_yS_z$/C (M = Co, Mo, Rh, or Re) class of chalcogenide electrocatalysts are exhibited in Fig. 3. $Co_xRu_yS_z$/C (SS), akin to the SS-synthesized Ru_xS_y/C material in Fig. 2, also bears the crystallographic

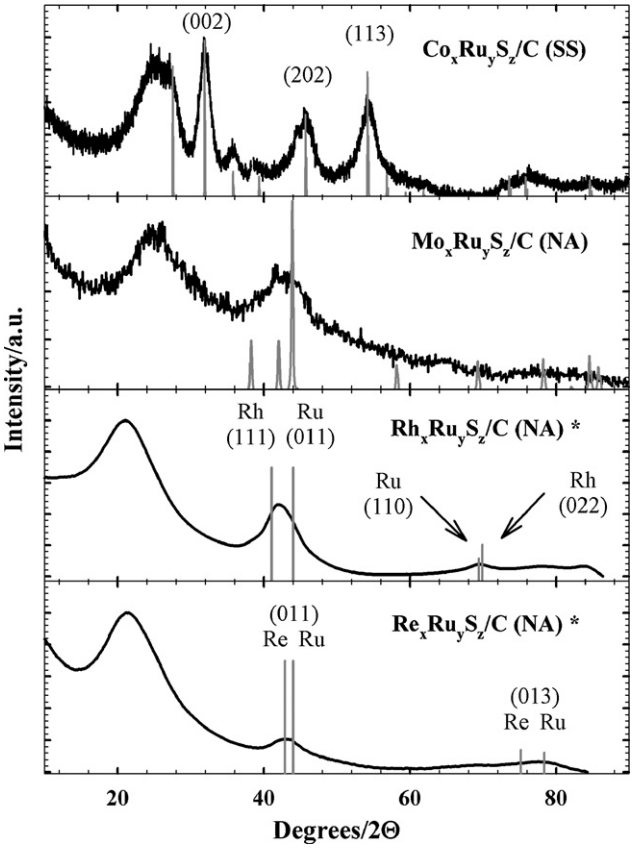

Fig. 3. Non-background-corrected powder X-ray diffractograms of 30 wt.% (top to bottom): $Co_xRu_yS_z$/C (SS), $Mo_xRu_yS_z$/C (NA), $Rh_xRu_yS_z$/C (NA), and $Re_xRu_yS_z$/C (NA). Cu Kα radiation, λ = 1.5406 Å, except for $Rh_xRu_yS_z$/C (NA)*, and $Re_xRu_yS_z$/C (NA)*, which were performed at beamline X-7B (NSLS) with monochromated 0.92137 Å radiation (adjusted to Cu Kα λ for comparative purposes).

fingerprint of *Pa*3 pyrite (grey lines). More significantly, the spectrum does not show evidence of unalloyed Co (fcc *Fm*3*m*) metal in the crystalline phase. Again, as observed with Ru_xS_y/C (SS), EDX indicates a non-stoichiometric M:S ratio of 1:2.3 (Table 1). In conjunction with the XRD results, the Co-based ternary cluster is most likely a Co-substituted pyrite phase. The final three diffractograms in Fig. 3 represent the NA-synthesized Mo, Rh, and Re-substituted Ru_xS_y/C (NA) chalcogenide electrocatalysts chosen on the basis of prior reports for ORR activity in PEM and DMFC applications [17–19,43,44]. The broad diffraction peaks observed for these materials point to their highly amorphous nature. The pattern for the $Mo_xRu_yS_z$ moiety shows a broad hcp Ru (0 1 1) peak (grey) without evidence of free Mo or Mo-oxide crystallites. Indexing to $P6_3/mmc$ (hcp Ru) resulted in a crystallite size of 2.2 nm.

In contrast to the $Mo_xRu_yS_z$/C (NA) data obtained on a laboratory Rigaku X-ray Diffractometer, the Rh and Re-containing NA materials were examined with high intensity synchrotron radiation at the NSLS at the high resolution X-ray diffraction beamline X-7B. Whereas only a broad hcp Ru (0 1 1) diffraction peak was observed for the $Mo_xRu_yS_z$, the higher resolution synchrotron diffractograms suggest that the Rh and Re-containing electrocatalysts are discreet mixtures of the involved metals. For example, the broad diffraction peak for $Rh_xRu_yS_z$/C (NA) exhibited at $2\theta = 42.03^\circ$ falls directly between the theoretical primary diffraction peaks for fcc Rh ((1 1 1) at 41.10°) and hcp Ru ((0 1 1) at 44.04°). This would suggest that the crystallites in this material are comprised of a mixture of discrete nanoparticles of Ru and Rh metal. Attempts to deconvolute the spectrum is further exacerbated by the overlapping presence of secondary diffraction peaks (Ru (1 1 0) at 69.47° and Rh (0 2 2) at 69.95°) at the only other observable diffraction peak at $2\theta = 69.77^\circ$. EDX analysis gave an atomic ratio of Rh:Ru of ∼1:1.5 (Table 1), and supports the hypothesis that the semi-crystalline portion of this electrocatalyst is a mixture of sulfur-coated Rh and Ru nanoparticles. Discriminating the different constituents for the $Re_xRu_yS_z$/C (NA) electrocatalyst (Fig. 3, bottom) is even more difficult because Re and Ru are both hcp ($P6_3/mmc$ space group) crystals. While indexing both the Rh and Re-containing Ru_xS_y/C (NA) electrocatalysts to hcp Ru gave a derived crystallite size of ∼2.2 nm, the particle size determinations for the ternary NA electrocatalysts (Table 1) should be taken as only a general conclusion. The materials are obviously amorphous (lacking long range order), and their respective sub-2.5 nm particle size places a limit on the accuracy of standard (and even synchrotron) powder X-ray diffraction. Despite these limitations, the synchrotron XRD patterns obtained for the $Rh_xRu_yS_z$ and $Rh_xRu_yS_z$ electrocatalysts gives strong evidence to the hypothesis that the low temperature NA synthetic route produces discrete sulfur-coated amorphous nanocrystallites of the respective metal-carbonyl precursors.

3.1.4. SEM studies

Representative high resolution SEM micrographs showing the differences in particle agglomeration and distribution as a function of synthetic methodology are presented in Fig. 4 with the results summarized in Table 1. Indicative of both the SF and

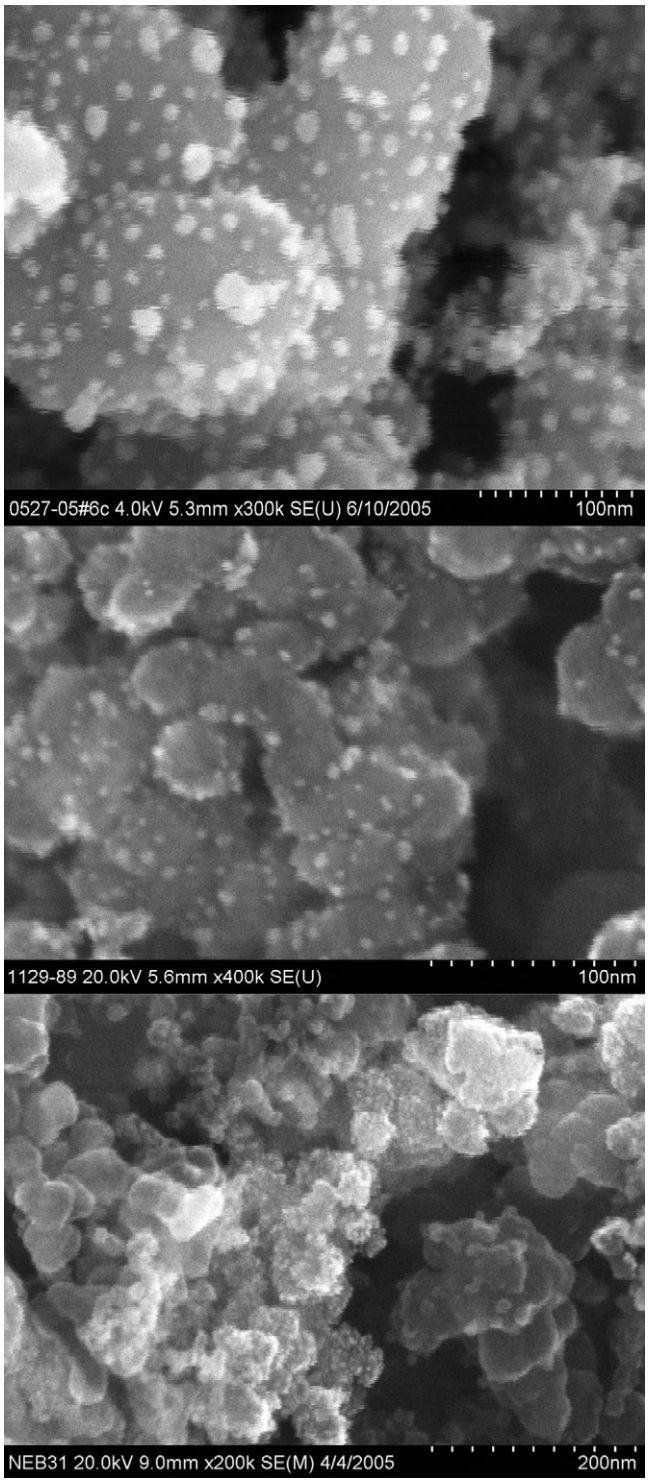

Fig. 4. Representative SEM micrographs of, top: 30 wt.% Rh_xS_y/C (AS), middle: 30 wt.% Ru_xS_y/C (SS), and bottom: 30 wt.% Rh_xS_y/C (NA).

AS methodology, the Rh_xS_y/C electrocatalysts show a distribution of agglomerates ranging in size from 10 to 30 nm. In contrast, the SS route produces a much narrower size range of ∼6–20 nm as evidenced both by the Ru_xS_y and $Co_xRu_yS_z$ electrocatalysts. These differences can be attributed to the thermal treatments involved in these synthetic methods. The SS method is typically performed at 400 °C whereas the AS and SF

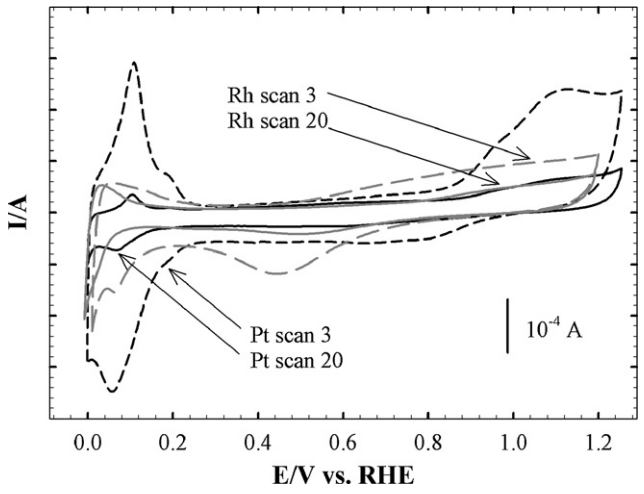

Fig. 5. Representative cyclic voltammograms of 30 wt.% Pt/C and Rh/C (both *E-TEK*) in de-aerated ($Ar_{(g)}$) room temperature 0.5 M HCl. Scan rate = 50 mV s^{-1}.

methods involve a post-synthesis thermal treatment of ~650 °C. This temperature increase results in greater particle growth for the AS/SF methodologies. In contrast, the NA-synthesized materials exhibit a narrow particle size range of 2–6 nm with little to no agglomeration. Our results are indicative of NA-synthesized materials, and agree well with numerous prior reports [17,40,41].

3.2. Cyclic voltammetry in 0.5 M HCl

3.2.1. 30 wt.% Pt/C and Rh/C standard electrocatalysts

The affinity for Cl_{ads}, and the detrimental effects this has on the ORR pathway, has been previously described for both Pt/C [4,45–47] and Rh/C [48,49] electrocatalysts. In 0.5 M HCl, Pt/C exhibits clear suppression of the adsorption/desorption of oxo-species by the third cycle (Fig. 5). Further, the site-blocking nature of Cl_{ads} on a polycrystalline Pt surface is seen to extend to the $H_{upd/opd}$ region. The widening of the electrochemical window of Cl_{ads} as a function of Cl^- concentration agrees with previously reported studies [4,47] albeit the prior work was conducted with much lower concentrations (1–100 mM) of Cl^-. By cycle 20, the cathodic PtO_x reduction peak has flattened out to a broad, shallow feature shifted by nearly −300 mV compared to the third scan. In addition the $H_{upd/opd}$ peaks (Pt(100)) are shifted to far more negative potentials which can be attributed to strong interactions arising from Cl_{ads} [50]. Akin to Pt/C, the Rh/C electrocatalyst exhibits severe deactivation after only 20 cycles in 0.5 M HCl (Fig. 5). Compared to an analogous Rh/C electrocatalyst in clean sulfuric acid (see Cao et al. [42] for a recent example) the adsorption/desorption of oxo-species is almost completely suppressed. The RhO_x reduction peak centered at ~500 mV is orders of magnitude smaller, and the prominent Rh(1 1 1) features in the hydrogen region are essentially eliminated [51,52]. The cyclic voltammograms for both electrocatalysts suggest that these materials exhibit a strong affinity for Cl_{ads}, and the adsorption of these ions impair the adsorption/desorption of the oxo-species necessary for ORR.

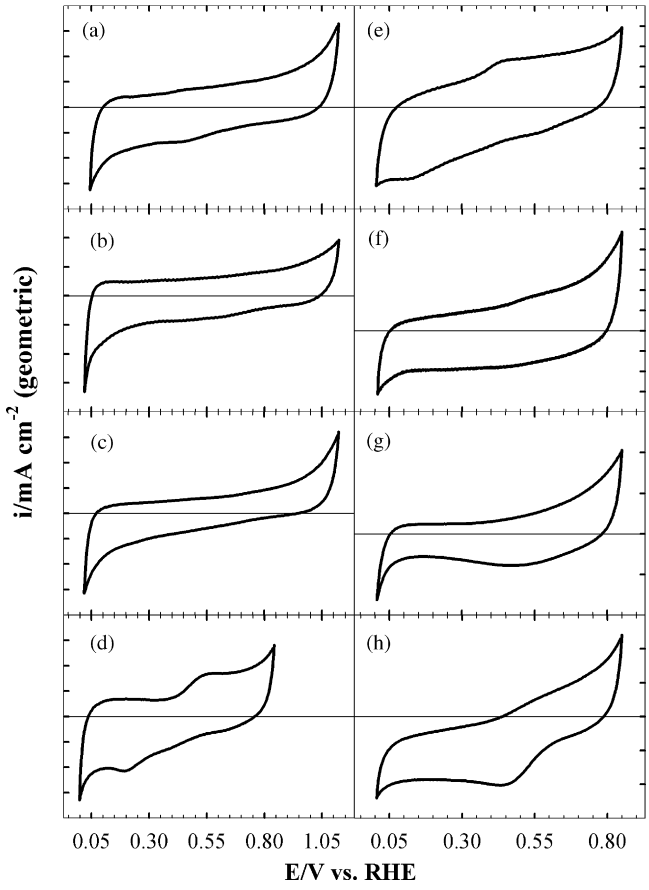

Fig. 6. Non IR-corrected cyclic voltammograms of the 30 wt.% chalcogenide electrocatalysts in room temperature de-aerated 0.5 M HCl: (a) Rh_xS_y/C (SF), (b) Rh_xS_y/C (AS), (c) Rh_xS_y/C (NA), (d) Ru_xS_y/C (SS), (e) $Co_xRu_yS_z$/C (SS), (f) $Mo_xRu_yS_z$/C (NA), (g) $Rh_xRu_yS_z$/C (NA), and (h) $Re_xRu_yS_z$/C (NA). All scan rates = 50 mV s^{-1}.

3.2.2. 30 wt.% chalcogenide electrocatalysts

Cyclic voltammograms (20 mV s^{-1}, de-aerated 0.5 M HCl) of the examined 30 wt.% chalcogenide electrocatalysts are shown in Fig. 6. As described in our recent publications [37,38] and others, [42] the Rh_xS_y/C SF and NA electrocatalysts (Fig. 6a and c) are essentially featureless in clean 0.5 M H_2SO_4 electrolyte despite their synthetic origins. While there is no clear evidence of a redox couple, Cao et al. [42] attributed the broad cathodic and anodic features in the Rh_xS_y/C (NA) CVs to oxidation and reduction processes involving the supporting H_2SO_4 electrolytes and sulfur surface layers. Such a conclusion is difficult to draw for the *E-TEK*-synthesized Rh_xS_y/C materials; for it has already been shown in the XRD section that these materials are not comprised of Rh nanoparticles, but are instead a balanced phase mixture of at least three Rh–S species. As these features cannot be assigned to sulfur overlayers, we therefore assign these features to oxidation and reduction processes of water and oxo-species on the Rh–S surfaces. Aside from evidence already obtained for water activation on the Rh_3S_4 phase of the SF material via *in situ* X-ray Absorption Spectroscopy studies, [37,38] the electrochemistry of the Rh_2S_3 and $Rh_{17}S_{15}$ phases are still ambiguous.

SS-synthesized Ru_xS_y and $Co_xRu_yS_z$ are presented in Fig. 6d and e, respectively. The XRD results showed that these catalysts possess a pyrite structure, and this is reflected in the voltammograms. Interestingly, while the Co-substituted pyrite material is considerably muted in comparison to the Ru_xS_y moiety, the onset potential of the broad anodic feature at ~0.40 V is unchanged. Most importantly, there is no evidence of a Co redox couple suggesting a complete incorporation of the Co into the pyrite matrix. The final sets of CVs ($Mo_xRu_yS_z$, $Rh_xRu_yS_z$, and $Re_xRu_yS_z$, all NA) are shown in Fig. 6f and h. These particular flavors of transition metal-doped Ru_xS_y (NA) electrocatalysts have been previously investigated by a number of other groups for PEMFC and DMFC cathode electrocatalysts [17,19,44,53,54]. Compared to the pyrite signatures (Fig. 6d and e), the NA-synthesized materials do not exhibit a clear interrelationship in peak positions and shapes. $Mo_xRu_yS_z$ (Fig. 6f) shows a broad cathodic feature centered at ~0.45 V, and features evidence of an adsorption phenomenon over the range of 0.45–0.70 V. Unlike prior reports, [53] there is no evidence of a Mo redox couple. As Mo is not known to easily incorporate into an hcp Ru crystal lattice, this gives evidence of a full passivation of the Mo by sulfur species. As with $Mo_xRu_yS_z$, the Rh and Re-containing materials (Fig. 6g and h) do not show clear redox couples involving the dopants. $Rh_xRu_yS_z$ shows a denser cathodic feature than the Mo-doped material, and smoothly tails up towards the oxygen evolution region on the anodic sweep. This is contrasted by the respective cathodic and anodic features of the $Re_xRu_yS_z$ material. Re forms a wide variety of ReO_x species in a hydrated environment, [55] and both our EDX studies (Table 1) and prior reports [19,44] suggest that the Re is not incorporated into the Ru_xS_y matrix as easily as Rh. Overall, the $Re_xRu_yS_z$ moiety exhibits a cathodic reduction wave beginning at ~0.60 V, while the Mo and Rh-doped materials exhibit much wider waves beginning up to a full 150 mV earlier. It is clear that the chemical nature of the sulfided "dopant" has an effect on the cyclic voltammograms.

3.3. RDE studies

3.3.1. Pt, Rh, and Rh–S materials

The effect of Cl_{ads} on the ORR kinetics of the Pt/C, Rh/C and Rh_xS_y/C electrocatalysts is displayed the RDE curves in Fig. 7. Cl_{ads} is well known poison for Pt electrocatalysts acting as a site blocking species preventing the adsorption of oxygen for ORR [46]. The ORR onset potential (qualitatively determined by a first derivative transform of the ORR curve) for the Pt electrocatalyst has been shifted negative by well over −300 mV. Further, the lack of a well defined limiting current can be attributed to strong Cl_{ads} adsorption, and this is indicative of all the electrocatalysts in this report. These experiments were performed in 0.5 M HCl, and it has been well established that the window of adsorption for Cl^- anions extends well into the H_{upd} region at much lower concentrations [4]. The Rh/C standard electrocatalyst is also severely depolarized by the Cl^- anions (on the order of −200 mV) although it exhibits a clear performance gain over the Pt electrocatalyst. Like the Pt/C electrocatalyst, strong Cl_{ads} interactions prevent the formation of a well defined limiting current. In addition, the reduction wave is singular, and does not exhibit kinks that could be associated with reduction processes outside of ORR. This lends credence to the commonly held hypothesis that Cl_{ads} affects ORR kinetics on these electrocatalysts by acting primarily as a site blocking species, and does not contribute to the overall reaction pathway [46,50].

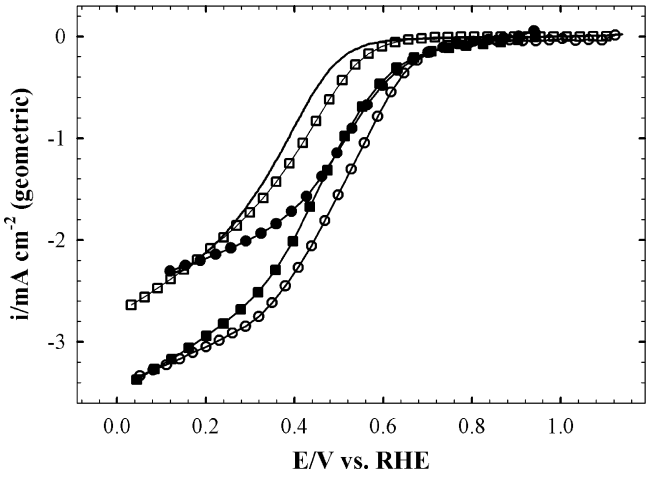

Fig. 7. ORR curves for the 30 wt.% Pt/C, Rh/C, and Rh-based chalcogenide electrocatalysts in room temperature O_2-saturated 0.5 M HCl:Pt/C—Rh/C (●) Rh_xS_y/C (SF) (○) Rh_xS_y/C (AS) (■), and Rh_xS_y/C (NA) (□). Rotation rate = 900 rpm and scan rate = 20 mV s^{-1}.

The effects of Cl_{ads} blocking the active sites for ORR are further reflected in the respective Tafel plots (Fig. 8). It should be mentioned that due to the lack of well-defined diffusion limiting currents these Tafel plots are not mass transfer-corrected. Both Pt and Rh/C exhibit a single Tafel slope in lieu of the usual 60/120 relationship exhibited in typical (halide anion free) acid electrolytes. The −60 mV dec^{-1} slope is generally agreed to arise from the adsorption of OH^- species congruent with water activation while the −120 mV dec^{-1} slope is attributed to ORR on a clean, adsorbate-free catalyst surface [23,56]. In O_2-saturated 0.5 M HCl electrolyte, neither Pt nor Rh/C shows the −60 mV dec^{-1} slope at low overpotentials. This does not

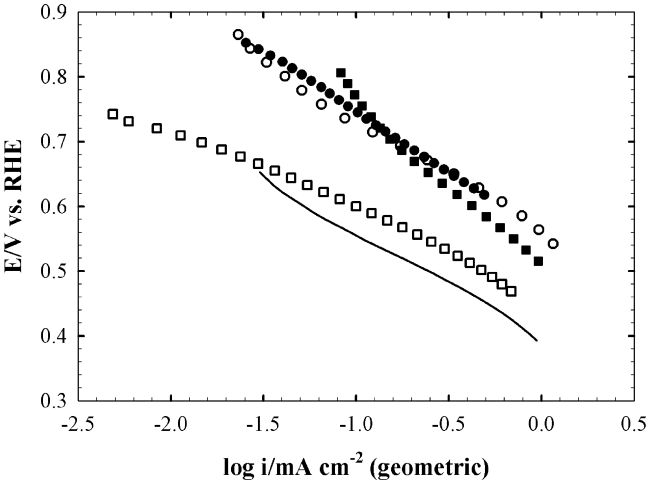

Fig. 8. Corresponding Tafel plots for the 30 wt.% Rh-based chalcogenide electrocatalysts in room temperature O_2-saturated 0.5 M HCl:Pt/C—Rh/C (●) Rh_xS_y/C (SF) (○) Rh_xS_y/C (AS) (■), and Rh_xS_y/C (NA) (□). Rotation rate = 900 rpm and scan rate = 20 mV s^{-1}.

mean that the catalyst surfaces are clean, but rather that Cl_{ads} is preventing the adsorption of OH species. This is more easily understood in light of the results of Li and Lipkowski who performed careful chronocoulometric studies to calculate the ΔG_{ads} of Cl^- and OH^- at 142 and 136 kJ mol^{-1}, respectively [50]. At higher overpotentials, oxygen is finally able to adsorb on the surface, and the slope approaches −120 mV dec^{-1} for both electrocatalysts. Due to omnipresent Cl_{ads}, however, the slopes for Pt and Rh/C are slightly higher at −159 and −186 mV dec^{-1}, respectively. These results mirror a recent report from Schmidt et al. [4] where an increase in the Tafel slope was related to the concentration of Cl^- anions in the electrolyte.

Overall, the general performance trend in Fig. 7 can be assigned as: Rh_xS_y (SF) > Rh > Rh_xS_y (AS) > Rh_xS_y (NA) > Pt although the differences are very small in some cases. For example, the AS material closely overlaps the kinetic region exhibited by the Rh/C electrocatalyst down to ∼0.50 V. The SF material, in contrast, shows a sharp performance increase relative to Rh/C beginning at 0.70 V. Previous ORR studies and activation energy determinations conducted on Rh_xS_y (SF) in 0.5 M H_2SO_4 [37] showed that the catalyst performs in a strikingly similar fashion to standard Pt electrocatalysts. Comparison with these previous results suggests that there is most likely some measure of Cl_{ads} on the active surface sites of the SF material. However, these effects are very small in comparison to the effects exhibited by Pt and Rh/C electrocatalysts. Rh_xS_y (NA) has been previously reported to be outperformed in ORR applications by Rh/C [42], and our results mirror those conclusions. However, it is evident that both the SF and AS-synthesized varieties of Rh_xS_y significantly outperform the NA-synthesized moiety, and the Rh_xS_y (SF) material exhibits a clear advantage over Rh/C under these conditions.

3.3.2. Ru-based chalcogenides

The ORR curves and derived Tafel plots for the Ru-based chalcogenide electrocatalysts in O_2-saturated 0.5 M HCl are presented in Figs. 9 and 10, respectively. As with the Rh-based

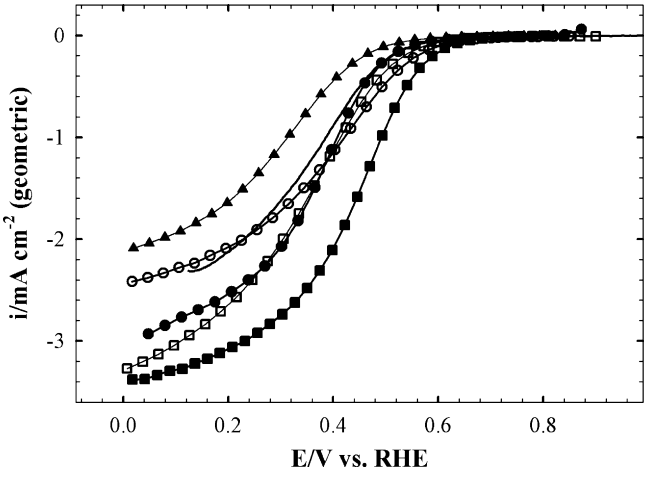

Fig. 9. ORR curves for the 30 wt.% Ru-based chalcogenide electrocatalysts in room temperature O_2-saturated 0.5 M HCl:Pt/C—$Co_xRu_yS_z$/C (SS) (●) $Mo_xRu_yS_z$/C (NA) (◯) $Rh_xRu_yS_z$/C (NA) (■) $Re_xRu_yS_z$/C (NA) (□), and Ru_xS_y/C (SS) (▲). Rotation rate = 900 rpm and scan rate = mV s^{-1}.

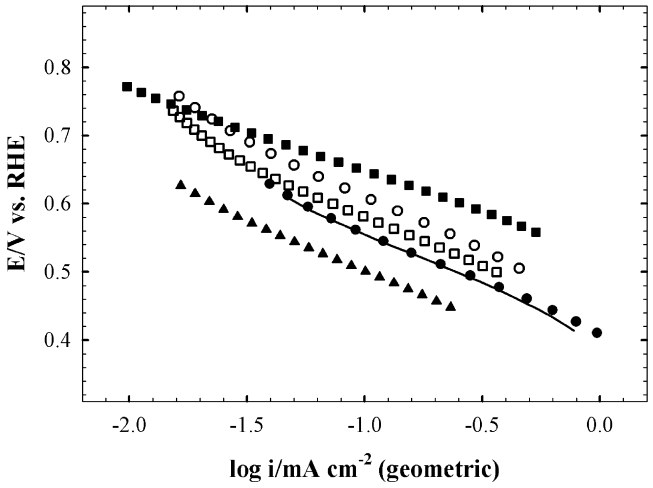

Fig. 10. Tafel plots for the 30 wt.% Ru-based chalcogenide electrocatalysts in room temperature O_2-saturated 0.5 M HCl:Pt/C—$Co_xRu_yS_z$/C (SS) (●) $Mo_xRu_yS_z$/C (NA) (◯) $Rh_xRu_yS_z$/C (NA) (■) $Re_xRu_yS_z$/C (NA) (□), and Ru_xS_y/C (SS) (▲). Rotation rate = 900 rpm, scan rate = 20 mV s^{-1}.

materials, the results are summarized in Table 2. On the basis of the derived E_{onset} for ORR and kinetic windows as displayed in Fig. 9, the following trend for ORR activity in 0.5 M HCl can be established: $Rh_xRu_yS_z$ (NA) ≫ {$Mo_xRu_yS_z$ (NA), $Re_xRu_yS_z$ (NA)} ≈ {$Co_xRu_yS_z$ (SS), Pt} > Ru_xS_y (SS). In respect to the SS-synthesized varieties (Ru_xS_y and $Co_xRu_yS_z$), while both materials exhibit an identical estimated onset potential of 0.64 V (Table 2), the addition of Co to the pyrite matrix offers a substantial performance gain in respect to current density. Tafel analysis of the ORR curves for these catalysts also revealed identical Tafel slopes of −150 mV dec^{-1} with the kinetic window for $Co_xRu_yS_z$ extending a full 60 mV farther than Ru_xS_y. The higher activity of the Co-doped material could be attributed to a synergistic effect akin to (a) a bifunctional effect where the Co is taking on the brunt of Cl_{ads} leaving Ru/Ru–S active site marginally freer to perform ORR, or (b) an electronic effect where the Co is changing the electronic density of the Ru/Ru–S active sites. These effects (in respect to water activation) have been observed for several species of PtM alloys, [23,56,57] but have yet to be reported for a chalcogenide electrocatalyst. Unfortunately, due to the concentration of the HCl used for the supporting electrolyte, it was impossible to carry out the necessary further studies (i.e., peroxide yield and electron transfer determinations via the rotating ring disk electrode method) due to the both the highly corrosive nature of the electrolyte and the potential of formation of $Cl_{2(g)}$ from Cl^- anions (1.36 V under standard acidic conditions). A full kinetic investigation (particularly the determination of the number of electrons transferred in uncontaminated electrolytes) is warranted, but is outside of the scope of this paper.

There is a clear division in the performance of the NA-synthesized ternary chalcogenide electrocatalysts with nominal differences between the Mo and Re-containing materials, and the $Rh_xRu_yS_z$ catalyst exhibiting the highest activity of the studied Ru-based catalysts (Fig. 9). Both $Mo_xRu_yS_z$ and $Re_xRu_yS_z$ perform marginally better than the standard Pt/C electrocata-

Table 2
Cumulative performance parameters for ORR at 900 rpm in room temperature oxygen-saturated 0.5 M HCl with derived Tafel slopes from the HCl electrolyzer cell shown for comparative purposes

30 wt.% Catalyst	ORR onset potential (V/RHE)[a]	*I*, density at 0.8/0.6/0.4 V (mA/cm^2)[b]	*b* (RDE) (mV/dec)	*b* (cell) (mV/dec)
Pt	0.62	N/A 0.050 0.89	−159	
Rh	0.88	0.046 0.47 1.68	−186	
Rh_xS_y (SF)	0.88	0.062 0.69 2.32	−158	−230
Rh_xS_y (AS)	0.86	0.082 0.42 1.98	−189	
Rh_xS_y (NA)	0.75	N/A 0.093 1.17	−126	
$Co_xRu_yS_z$ (SS)	0.64	N/A 0.053 1.07	−150	−249
$Mo_xRu_yS_z$ (NA)	0.77	N/A 0.10 1.15	−167	
$Rh_xRu_yS_z$ (NA)	0.78	NA 0.16 2.09	−121	
$Re_xRu_yS_z$ (NA)	0.74	N/A 0.068 1.13	−160	
Ru_xS_y (SS)	0.64	N/A 0.022 0.44	−151	−347

[a] Determined by first derivative analysis of the ORR curves.
[b] Geometric area, all potentials vs. RHE.

lyst, both in terms of onset potential and Tafel analysis, with the $Mo_xRu_yS_z$ electrocatalyst exhibiting slightly higher activity. Unlike the crystalline SS-synthesized $Co_xRu_yS_z$ ternary material, these catalysts are comprised of discrete sulfur-coated metal nanoparticles. EDX of the as-synthesized catalysts showed that there was initially less at% Re:Ru than Mo:Ru. This is in agreement with the studies of Reeve et al. [44] where it was observed that a fair amount of the "dopants" corrode and dissolve out of the catalyst system. This unfortunate byproduct of NA-synthesized electrocatalysts means that after electrochemical activation, both the Mo and Re-doped materials are essentially Ru_xS_y catalysts. This would explain the similarities in both the current densities in the kinetic region as well as the identical $-150\,mV\,dec^{-1}$ Tafel slopes.

The activity of the $Rh_xRu_yS_z$ can be described as a mixture of the properties of both the $Mo_xRu_yS_z$ and Rh_xS_y (NA) analogs. Like the Mo and Re-containing materials, the higher activity correlates with mixing two transition metals. However, certain kinetic parameters, particularly the Tafel slope of $-121\,mV\,dec^{-1}$, correlates closely with the derived value for the Rh_xS_y (NA) electrocatalyst as summarized in Table 2. While possessing similar Tafel slopes traditionally corresponding to an efficient, oxide-free Pt surface for ORR, the higher current densities for $Rh_xRu_yS_z$ versus Rh_xS_y (both NA) suggests that the sulfur-passivated Ru nanoparticles are more active towards ORR in Cl-saturated environments than sulfur-passivated Rh nanoparticle analogs. This indicates that the incorporated Rh is shielding the ORR-active Ru_xS_y nanoparticles from the depolarizing effects of adsorbed Cl^- species.

3.4. Chlorine generation cells

While the RDE studies were conducted in a corrosive 0.5 M HCl environment, the true test of performance involves ORR in an industrial chlorine-saturated HCl concentration cell. In light of the observed performance trends in respect to synthetic methodology, two electrodes comprised of 30 wt.% Ru_xS_y/C and $Co_xRu_yS_z$/C (both SS) were individually tested as oxygen-consuming cathodes for hydrochloric acid electrolysis against a standard DSA anode, and compared to a state-of-the-art GDE

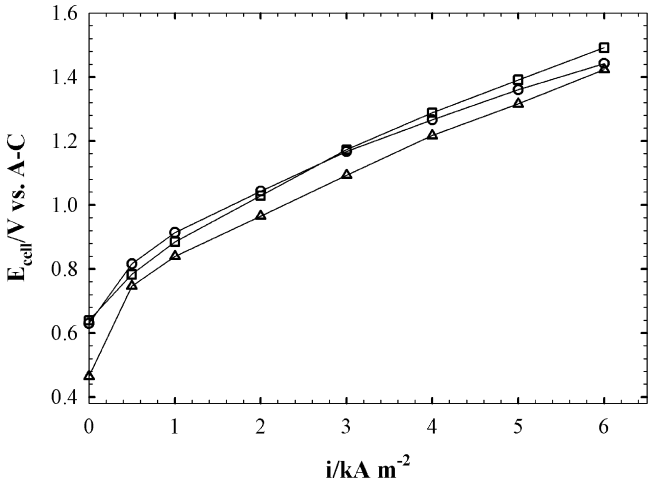

Fig. 11. Polarization curves for the HCl Electrolyzer Cell run in constant current mode: Rh_xS_y (SF) (△), $Co_xRu_yS_z$ (SS) (◯), and Ru_xS_y (SS) (□). Cell temperature = 55 °C, back pressure = 2 atm.

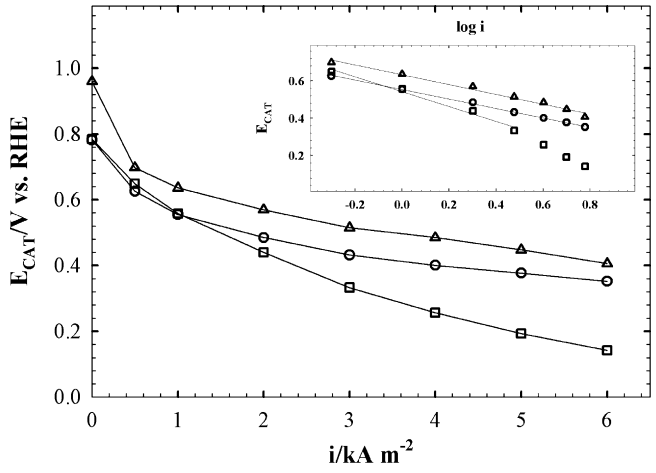

Fig. 12. Cathodic portion of the HCl Electrolyzer Cell run in constant current mode: Rh_xS_y (SF) (△) $Co_xRu_yS_z$ (SS) (◯), and Ru_xS_y (SS) (□). Inset: derived Tafel slopes. Cell temperature = 55 °C and back pressure = 2 atm.

incorporating 30 wt.% Rh_xS_y/C (SF). While the NA-synthesized $Rh_xRu_yS_z$ electrocatalyst exhibited promising performance in the RDE studies, it was impossible to evaluate in the electrolyzer cell. While it was possible to evaluate deposited thin films of the NA-synthesized materials in room temperature 0.5 M HCl, the materials dissolved in the warm (55 °C) +5 M HCl electrolyte upon irreversible shutdown. In the case of the Ru-based NA electrocatalysts, this was observed as a color change to light blue of the cathode drain feed.

Their removal from the GDE is most likely a result (or combination) of two factors. First, the NA materials are of a significantly smaller particle size (see Table 1) than the *E-TEK* materials. This is perhaps best illustrated by the relative stability of the *E-TEK* Rh/C electrocatalyst (at three times the particle size of the NA materials). The second reason could be attributed to the nature of the metal-sulfur interactions. Whereas the *E-TEK* materials possess complex metal-S crystallinity, the NA-synthesized materials are more akin to sulfur-passivated nanoparticles which lack any long range order in the metal-sulfur bonding. In either case the instability of the NA materials in the heated (55 °C) 5 M HCl electrolyte is perhaps best illustrated by the fact that after this dissolution was initially observed, the electrolyzer cell electrolyte was employed as a highly effective cleaner for the NA synthesis glassware to remove any residual metals. Thus, while the halide anion adsorption tolerance of the NA-synthesized chalcogenide materials is significant in comparison to the current state of the art noble metal electrocatalysts for fuel cell applications, they are not a viable option for ODC chlorine generation applications.

Fig. 11 presents a comparison of full chlorine electrolyzer cell polarization curves with Ru_xS_y (SS), $Co_xRu_yS_z$ (SS), and Rh_xS_y (SF) cathodes. The Rh_xS_y (SF) cathode-based cell results in a total cell potential nearly 100 mV lower than the SS-synthesized cathodes at 3 kA m^{-2}. Both the Ru_xS_y and $Co_xRu_yS_z$ cathodes result in a cell with closely mirrored performance although the $Co_xRu_yS_z$ cathode offers a slight performance gain at low and high current densities. In particular, the performance of the SS-based cells closely mimics the results from the RDE studies. Both materials exhibit nearly identical performance at low current densities (particular to the cell studies is the identical OCP_{CELL} values of 0.64 V).

The derived performance of the chalcogenide cathodes in an operating electrolyzer cell is expressed in Fig. 12. These curves can be considered analogous to the cathodic portion PEMFC polarization curves with the following exceptions: (1) these are driven cells (e.g., always under full electrolytic control), (2) the cathode chamber *always* contains residual HCl via crossover from the anode compartment, and (3) while the concentration of HCl in the cathode compartment is proportional to the current density the maximum concentration at 6 kA m^{-2} is less than 50 mM. As seen in the overall cell polarization curves (Fig. 11), Rh_xS_y (SF) offers undisputed superior activity compared to the SS-synthesized catalysts. $Co_xRu_yS_z$ represents the closest competitor with a 100 mV loss compared to Rh_xS_y (SF) over the range of 1–5 kA m^{-2}. Both Ru_xS_y (SS) and $Co_xRu_yS_z$ (SS) perform identically from OCP to ~2 kA m^{-2}, where the Ru_xS_y begins to exhibit a considerable drop in performance. That the addition of Co to the Ru_xS_y (SS) crystal matrix improves the ORR kinetics supports the postulate from the RDE studies in 0.5 M HCl: the $Co_xRu_yS_z$ (SS) chalcogenide electrocatalyst shows a clear performance gain over the Ru_xS_y (SS) electrocatalyst proffered most likely by a bi-functional effect from the incorporated Co transition metal.

The inset in Fig. 12 represents the derived Tafel slopes from the cathode polarization curves, and the values are offered for comparison with those obtained from the RDE studies in Table 2. None of the materials exhibit the theoretical $-120\,mV\,dec^{-1}$ slope which generally indicates full $4e^-$ ORR on a clean electrode surface. Both the Rh_xS_y (SF) and $Co_xRu_yS_z$ (SS) material deviate considerably from the RDE-derived slopes ($-150\,mV\,dec^{-1}$) with cell-derived Tafel slopes of $-240\,mV\,dec^{-1}$. The Ru_xS_y (SS) shows a considerably higher Tafel slope of $-347\,mV\,dec^{-1}$ over a smaller current density range than for the Rh_xS_y (SF) and $Co_xRu_yS_z$ (SS) electrocatalysts, and constantly increases beyond 3 kA m^{-2}.

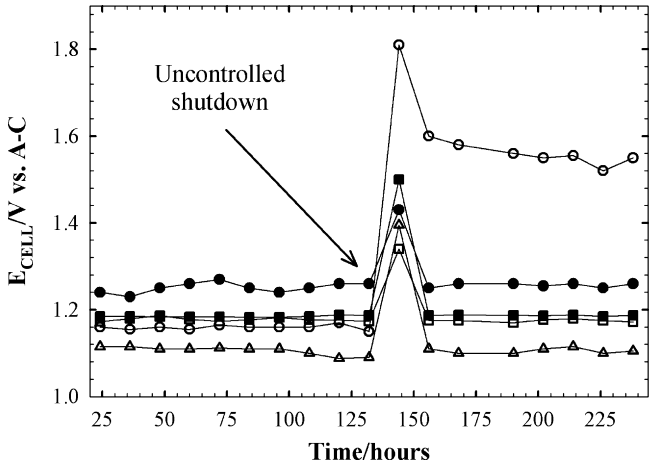

Fig. 13. HCl Electrolyzer cell performance with 30 wt.%: Pt/C (◯), Rh/C (●), $Co_xRu_yS_z$/C (SS) (□), Ru_xS_y/C (SS) (■), and Rh_xS_y/C (SF) (△). Constant current = 3 kA m^{-2} and cell temperature = 55 °C, back pressure = 2 atm.

Because the concentration of HCl in the cathode compartment of the electrolyzer cell is at least 10 times lower than that in the RDE studies, a direct comparison of the Tafel values would be somewhat disingenuous. Despite the fact that it was impossible to determine the respective peroxide yields for the electrocatalysts, there is some significance to the Tafel slope values from the cell data. This could represent either an increase in peroxide production ($2e^-$ transfer versus $1e^-$ for facile ORR), or a shift in the transfer coefficient. Unfortunately, it was impossible to determine the peroxide yields in either the RDE or electrolyzer cell experiments.

In order to truly determine the viability of the chalcogenide ODCs, their respective performance and recovery from an uncontrolled shutdown was examined (Fig. 13). The electrodes were operated at 3 kA m^{-2} for 132 h, and the load was instantaneously removed. This resulted in the ODC compartment flooding with hot ∼5 M HCl in the presence of oxygen. The oxygen flow was then shut off, and the cells were allowed to sit for 12 h at room temperature. At start up all of the ODCs show a significant depolarization as compared to the final cell potential before the shutdown. With the exception of the Pt ODC, however, the chalcogenides and the Rh electrocatalyst gradually recover their pre-shutdown potentials. The cell incorporating the Pt catalyst has increased from 1.06 to ∼1.5 V giving evidence to irreversible depolarization. In an industrial setting, this result would require the time consuming replacement of the Pt ODCs which is especially relevant in the context of the scale of operation of HCl electrolyzers (typically hundreds of cells would have to be modified). In particular, the Ru_xS_y (SS) and $Co_xRu_yS_z$ (SS) electrocatalysts return to their pre-shutdown cell potentials, and can therefore be considered as suitably stable for operation as ODC cathodes even after an uncontrolled shutdown.

4. Conclusions

Compared to state of the art Pt/C and Rh/C, chalcogenide electrocatalysts were found to exhibit a surprising level of resistance to Cl^- attack in 0.5 M HCl RDE experiments. In general, the performance of the chalcogenide materials was found to depend strongly on both their synthetic origins. Materials synthesized by the new methods developed by *E-TEK* and De Nora yield crystalline agglomerates which exhibit increased stability and kinetics for ORR over the traditional non-aqueous-synthesized electrocatalysts. In addition, while all of the examined varieties outperformed Pt in 0.5 M HCl RDE tests, the non-aqueous varieties, most likely as a result of their sub-4 nm particle sizes, were unable to operate as oxygen-depolarized cathodes in a true HCl electrolyzer cell environment owing to irreversible dissolution. Solid-state synthesized $Co_xRu_yS_z$ and Ru_xS_y both outperformed Pt/C and Rh/C in the electrolyzer cell, but lagged behind the state of the art Rh_xS_y/C electrocatalyst developed primarily for this application. None the less, the Ru-based materials were not irreversibly depolarized as a result of an uncontrolled shutdown. Considering that ruthenium is ∼7 times less expensive than rhodium, these Ru-based materials may present a viable alternative to expensive Rh_xS_y systems for the ODC HCl electrolysis industry.

Acknowledgements

This work has been accomplished thanks to the financial and intellectual support of the Industrie De Nora (IDN) and the *E-TEK* division of PEMEAS Fuel Cell Technologies, Inc. (NJ) and it is registered with the Office of Patents and Trademarks under the following numbers; US 6,967,185, US 6,149,782 and U.S. 6,358,381. The authors wish to gratefully thank Dr. Hakim Nazih (Northeastern University) for his collaboration during the collection of the SEM micro-graph data, and Dr. Wen Wen (Chemistry Dept, Brookhaven National Labs) for collecting the X-ray diffraction data at the National Synchrotron Light Source (beamline X-7B). Use of the National Synchrotron Light Source, Brookhaven National Laboratory, was supported by the U.S. Department of Energy, Office of Science, Office of Basic Energy Sciences, under Contract No. DE-AC02-98CH10886.

References

[1] E.J. Moniz, J.D. Baldeschwieler, Report of a Joint Workshop Exploring the Role of the Mathematical and Physical Sciences in Support of Basic Research Needs of the US Intelligence Community, National Science Foundation, Washington, DC, 2003, 52 pp., www.nsf.gov/attachments/102809/public/, March 16, 2005.
[2] F. Gestermann, A. Ottaviani, in: J. Moorhouse (Ed.), Modern Chlor-Alkali Technology, vol. 8, SCI, London, 2001, p. 49.
[3] F. Federico, G.N. Martelli, D. Pinter, in: J. Moorhouse (Ed.), Modern Chlor-alkali Technology, vol. 8, SCI, London, 2001, p. 114.
[4] T.J. Schmidt, U.A. Paulus, H.A. Gasteiger, R.J. Behm, J. Electroanal. Chem. 508 (2001) 41.
[5] R.J. Allen, J.R. Giallombardo, D. Czerwiec, E.S. De Castro, K. Shaikh, F. Gestermann, H.-D. Pinter, G. Speer, De Nora Elettrodi S.p.A. (IT); Bayer A.-G. (DE), US 6,402,930, 2002.
[6] R.J. Allen, J.R. Giallombardo, D. Czerwiec, E.S. De Castro, K. Shaikh, De Nora S.p.A (IT), US 6,149,782, 2000.
[7] R.J. Allen, J.R. Giallombardo, D. Czerwiec, E.S. De Castro, K. Shaikh, De Nora S.p.A. (IT), US 6,358,381, 2002.
[8] http://chemicalprocessing.com/, Bayer charges ahead with novel cathode, http://www.chemicalprocessing.com/, industrynews/2006/060.html - related_info, November 21, 2006.

[9] Johnson-Matthey, The Platinum Metals Report: February 2007 Price Report, http://www.platinum.matthey.com/uploaded_files/pricereport0207.pdf, April 7, 2007.
[10] J.A. De los Reyes, S. Gobolos, M. Vrinat, M. Breysse, Catal. Lett. 5 (1990) 17.
[11] A.F. Gullá, R.J. Allen, E.S. De Castro, De Nora Elettrodi, S.p.A. (IT), WO 2004/106591, 2005.
[12] T.G. Harvey, T.W. Matheson, J. Catal. 101 (1986) 253.
[13] J.D. Passaretti, R.R. Chianelli, A. Wold, K. Dwight, J. Covino, J. Solid State Chem. 64 (1986) 365.
[14] N. Alonso Vante, H. Tributsch, Nature 323 (1986) 431.
[15] N. Alonso Vante, B. Schubert, H. Tributsch, A. Perrin, J. Catal. 112 (1988) 384.
[16] O. Solorza-Feria, K. Ellmer, M. Giersig, N. Alonso-Vante, Electrochim. Acta 39 (1994) 1647.
[17] N. Alonso-Vante, in: A. Wieckowski, E.R. Savinova, C.G. Vayenas (Eds.), Catalysis and Electrocatalysis at Nanoparticle Surfaces, Marcel Dekker, New York, 2003, p. 931.
[18] A.K. Shukla, R.K. Raman, Annu. Rev. Mater. Res. 33 (2003) 155.
[19] R.W. Reeve, P.A. Christensen, A.J. Dickinson, A. Hamnett, K. Scott, Electrochim. Acta 45 (2000) 4237.
[20] H. Tributsch, M. Bron, M. Hilgendorff, H. Schulenburg, I. Dorbandt, V. Eyert, P. Bogdanoff, S. Fiechter, J. Appl. Electrochem. 31 (2001) 739.
[21] Y.M. Tsou, H. Deng, G.N. Martelli, R.J. Allen, E.S. De Castro, De Nora Elettrodi S.p.A. (IT), US 6,855,660, 2005.
[22] R.J. Allen A.F. Gullá, De Nora Elettrodi S.p.A., (IT), US 6,967,185, 2005.
[23] V.S. Murthi, R.C. Urian, S. Mukerjee, J. Phys. Chem. B 108 (2004) 11011.
[24] U.A. Paulus, T.J. Schmidt, H.A. Gasteiger, R.J. Behm, J. Electroanal. Chem. 495 (2001) 134.
[25] T.J. Schmidt, H.A. Gasteiger, R.J. Behm, Electrochem. Commun. 1 (1999) 1.
[26] H.B. Beer, H.B. Beer, GB 1147442, 1965.
[27] H.B. Beer, J. Electrochem. Soc. 127 (1980) 303C.
[28] P.C.S. Hayfield, Platinum Metal Rev. 42 (1998) 116.
[29] P.C.S. Hayfield, Platinum Metal Rev. 42 (1998) 46.
[30] E.N. Balko, General Electric Co., US 4,311,568, 1982.
[31] E.N. Balko, General Electric Co., US 4,294,671, 1981.
[32] J. Beck, T. Hilbert, Z. Anorg. Allg. Chem. 626 (2000) 72.
[33] E. Parthe, D.K. Hohnke, F. Hulliger, Acta Cryst. 23 (1967) 832.
[34] R. Juza, O. Hülsmann, K. Meisel, W. Biltz, Z. Anorg. Allg. Chem. 225 (1935) 369.
[35] S. Geller, Acta Cryst. 15 (1962) 1198.
[36] S. Geller, Acta Cryst. 15 (1962) 713.
[37] J.M. Ziegelbauer, D. Gatewood, A.F. Gullá, D.E. Ramaker, S. Mukerjee, Electrochem. Solid-State Lett. 9 (2006) A430.
[38] J.M. Ziegelbauer, D. Gatewood, D.E. Ramaker, S. Mukerjee, ECS Trans. 1 (2005) 119.
[39] A.F. Gullá, L. Gancs, R.J. Allen, S. Mukerjee, Appl. Catal. A: General (2007), doi:10.1016/j.apcata.2007.04.013.
[40] S. Bastide, C. Levy-Clement, A. Albu-Yaron, A.C. Boucher, N. Alonso-Vante, Electrochem. Solid-State Lett. 3 (2000) 450.
[41] F. Dassenoy, W. Vogel, N. Alonso-Vante, J. Phys. Chem. B 106 (2002) 12152.
[42] D. Cao, A. Wieckowski, J. Inukai, N. Alonso-Vante, J. Electrochem. Soc. 153 (2006) A869.
[43] N. Alonso-Vante, I.V. Malakhov, S.G. Nikitenko, E.R. Savinova, D.I. Kochubey, Electrochim. Acta 47 (2002) 3807.
[44] R.W. Reeve, P.A. Christensen, A. Hamnett, S.A. Haydock, S.C. Roy, J. Electrochem. Soc. 145 (1998) 3463.
[45] C.A. Lucas, N.M. Marković, P.N. Ross, Phys. Rev. B 55 (1997) 7964.
[46] N.M. Marković, P.N. Ross, Surf. Sci. Rep. 45 (2002) 117.
[47] V. Stamenković, N.M. Marković, P.N. Ross, J. Electroanal. Chem. 500 (2001) 44.
[48] G. Horanyi, E.M. Rizmayer, J. Electroanal. Chem. 198 (1986) 379.
[49] M. Hourani, A. Weickowski, J. Electroanal. Chem. 244 (1988) 147.
[50] N. Li, J. Lipkowski, J. Electroanal. Chem. 2000 (2000) 95.
[51] C.K. Rhee, M. Wasberg, P. Zelenay, A. Wieckowski, Catal. Lett. 10 (1991) 149.
[52] G. Horanyi, M. Wasberg, J. Electroanal. Chem. 404 (1996) 291.
[53] V. Trapp, P. Christensen, A. Hamnett, J. Chem. Soc., Faraday Trans. 92 (1996) 4311.
[54] N. Alonso-Vante, M. Fieber-Erdmann, H. Rossner, E. Holub-Krappe, C. Giorgetti, A. Tadjeddine, E. Dartyge, A. Fontaine, R. Frahm, J. Phys. IV 7 (1997) 887.
[55] M. Pourbaix, Atlas of Electrochemical Equilibria in Aqueous Solutions, Pergamon Press, London, 1966, p. 350.
[56] S. Mukerjee, R.C. Urian, Electrochim. Acta 47 (2002) 3219.
[57] S. Mukerjee, R.C. Urian, C.K. Witham, T.I. Valdez, S.R. Narayanan, Direct Methanol Fuel Cells, vol. PV 2001-4, The Electrochemical Society Proceedings Series, Pennington, NJ, 2001, p. 136.